Received January 2001
Revised May 2001
Accepted June 2001

Impingement cooling in a rib-roughened channel with cross-flow

Rongguang Jia, Masoud Rokni and Bengt Sundén
Division of Heat Transfer, Lund Institute of Technology, Lund, Sweden

Keywords *Heat transfer, Turbulence, Surface roughness*

Abstract *A numerical investigation to determine the velocity and heat transfer characteristics of multiple impinging slot jets in rib-roughened channels in the presence of cross-flow has been carried out. Fluid flow is modeled using an explicit algebraic stress model. A simple eddy diffusivity and a generalized gradient diffusion hypothesis are applied for the modeling of turbulent heat fluxes. The computations are validated against available experimental fluid flow and heat transfer data. Different size and arrangement of jets and ribs are considered in detail, while the Reynolds numbers of a jet and the channel inlet are fixed at 6,000 and 14,000, respectively. Results show that the ratio (B/W) between the size of the jets and ribs is most important. An explanation is that the ribs inhibit the motion of eddies by preventing them from coming very close to the surface when B/W is low, e.g. B/W = 1, although the ribs will increase the turbulence intensity. This blockage limited the heat transfer enhancement effect of the ribs and impinging jets.*

Nomenclature

b_{ij}	= anisotropy tensor	T	= temperature
B	= width of a slot jet nozzle	$\overline{u_i u_j}$	= turbulent stresses
De	= the diameter of an axisymmetric jet, giving the same cross-sectional area as the slot jet under investigation	$\overline{u_j t}$	= turbulent heat fluxes
		U_j	= velocity
		V_{in}	= inlet velocity of impinging slot jet
E	= height of a rib	W	= width of a rib, m
f_1, f_2, f_μ, f_μ^T	= damping functions	W_{ij}	= mean vorticity
H	= nozzle-to-wall distance or channel height	y^+	= normal distance to the wall, $y^+ = \rho U^* \zeta / \mu$
I	= turbulence intensity	Γ	= numerical diffusivity
k	= turbulent kinetic energy	δ_{ij}	= Kronecker delta
Nu	= local Nusselt number	ε	= eddy dissipation rate
Nu_s	= local Nusselt number in smooth channel	ζ	= distance normal to the wall
		η	= invariant coefficient in Eq. (8)
$\overline{Nu}$	= average Nusselt number	μ	= molecular viscosity
P	= pressure, or pitch of the ribs or jets	μ_τ	= turbulent viscosity
		ρ	= density
Pr	= Prandtl number	σ	= turbulent Prandtl number
S_{ij}	= mean strain rate	Φ	= variable
S_Φ	= source term for variable Φ	ξ	= invariant coefficient in Eq. (8)

International Journal of Numerical Methods for Heat & Fluid Flow, Vol. 11 No. 7, 2001, pp. 642-662.

The Swedish Energy Administration (STEM) financially supported this research work.

1. Introduction

Because jet impinging normally to a wall can remove a large amount of heat over a relatively small surface area, this flow geometry has been used in various industrial applications, especially in cooling the walls of high temperature thermal systems. However, the high heat transfer coefficient of a single jet decays rapidly with the increase of distance downstream of the stagnation point, and one way to enhance the heat transfer in this region is to roughen the walls with ribs and/or to use multiple impinging jets. In addition, the surface that needs to be cooled may become roughened due to unavoidable wear, corrosion or contamination. Therefore, it is important to understand the effect of surface roughness on the impinging heat transfer along a rough wall. In the present study, heat transfer of multiple impinging slot-jets along a rib-roughened channel is considered. This can be regarded as a combination of multiple impingement jets cooling and turbulent cooling in a rib-roughened channel. Such heat transfer processes occur in combustor wall cooling and leading edge cooling of gas turbine blades.

The impingement cooling jet from a single rectangular (slot) or round nozzle or array of nozzles over a heated surface has been studied extensively in the past due to its wide application. This is also true for rib-roughened channels. Therefore, it is almost impossible to review all articles.

With regard to slot impinging jets, Looney and Walsh (1984) presented an early survey of the literature on heat and flow characteristics of slot jets. More recent measurements have been made by Ichimiya and Hosaka (1992), Ashforth-Frost *et al.* (1997), and Lin *et al.* (1997). Numerical investigations have been carried out by Seyedein *et al.* (1995), Chen and Modi (1999), etc. According to their studies, several conclusions can be drawn. For example:

- Stagnation heat transfer characteristics are very sensitive to the jet velocity profile and turbulence intensity at the slot-nozzle exit.
- Local Nusselt number reaches its maximum at the stagnation region when H/B = 6, where H and B are defined in Figure 1.
- There is a second maximum of Nusselt number when H/B < 5.
- The length of the potential core is 6B for unconfined impinging slot jets, 6.5B for confined impinging slot jets, if a 95 per cent criterion is used.
- There is a marked increase of u'/V_{in} very close to the impingement wall, which arises from the shear induced by the flow acceleration away from the stagnation point.
- Models predicting the mean flow poorly also predict the turbulent quantities poorly, and vice versa.

Concerning heat and fluid flow in rib-roughened channels, Liu *et al.* (1993) experimentally investigated the fully developed heat and fluid flow behavior in rectangular rib-roughened channels. Tsai *et al.* (2000) evaluated five low Reynolds number turbulence models for the prediction of fully developed fluid

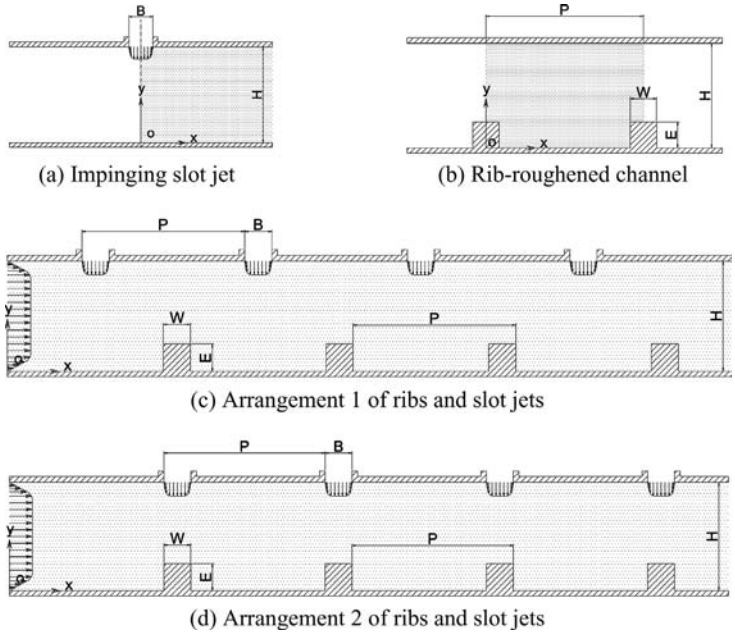

Figure 1.
Sketch of the calculation domains used in different cases

flow in an asymmetric-ribbed channel against experimental results from Liu *et al.* (1993). Yap correction was also added to some of these models. Durbin's (1995) model with Yap correction performed best among these five models, but the prediction of the Nusselt number between the ribs was not satisfactory. Saidi and Sundén (2000) studied the turbulent convective heat transfer in 3D rib-roughened channels, using a simple eddy viscosity model (EVM) and an explicit algebraic stress model (EASM). As reported, the EASM has some superiority over the EVM in prediction of the velocity field, but the mean thermal predictions are not very different.

Considering the large body of available literature on the heat and fluid flow of impinging jets and rib-roughened channels, it is surprising that there are very few studies reporting the multiple impinging jets over rib-roughened surfaces with cross-flow, because such cases occur in gas turbine applications, as mentioned above.

The aim of the present work is to provide a numerical study of the impingement cooling over rib-roughened walls with cross-flow, using an explicit algebraic stress model (EASM) (Rokni, 2000), to find the optimum configuration of ribs, jets, and cross-flow.

In the present study, three simplified cases are used to validate the model and computer code against the available experimental data (Figure 1), and then different configurations are studied to find the optimum.

2. Method

2.1 Basic equations

The time-averaged fluid flow is solved using the Reynolds-averaged Navier-Stokes (RANS) equations:

$$\frac{\partial \rho}{\partial t} + \frac{\partial}{\partial x_j}(\rho U_j) = 0 \tag{1}$$

$$\frac{\partial(\rho U_i)}{\partial t} + \frac{\partial}{\partial x_j}(\rho U_i U_j) = -\frac{\partial P}{\partial x_i} + \frac{\partial}{\partial x_j}\left[\mu\left(\frac{\partial U_i}{\partial x_j} + \frac{\partial U_j}{\partial x_i}\right)\right] + \frac{\partial}{\partial x_j}(-\rho\overline{u_i u_j}) \tag{2}$$

$$\frac{\partial(\rho T)}{\partial t} + \frac{\partial}{\partial x_j}(\rho U_j T) = \frac{\partial}{\partial x_j}\left[\frac{\mu}{\mathrm{Pr}}\frac{\partial T}{\partial x_j}\right] + \frac{\partial}{\partial x_j}(-\rho\overline{u_j t}) \tag{3}$$

The turbulent stresses $-\rho\overline{u_i u_j}$ and turbulent heat fluxes $\rho c_p \overline{u_j t}$ require modeling in order to close the equations. An EASM turbulence model will be used for the turbulent stresses, and the turbulent heat fluxes will be modeled using simple eddy diffusivity and gradient diffusion types models. The fluid properties are assumed to be constants.

2.2 Turbulence models

2.2.1 Modeling of Reynolds stresses. Algebraic stress models (ASM) originate from Reynolds stress closures under assumptions about the convective and diffusive terms (see, for example, Gatski and Speziale, 1993). The result is an implicit algebraic equation for the anisotropic Reynolds stresses b_{ij}. Since such a representation is implicit, the numerical robustness of its solution can be questionable. The EASM used here replaces this implicit relation with a polynomial expansion in a tensor basis. In two-dimensional flows, the three-term basis used here is exact, while in three-dimensional flows it is taken as a low-order approximation to the full ten-term basis. In addition, a linear pressure-strain rate correlation model and an isotropic dissipation rate are assumed. The EASM used here is the revised version described by Rokni (2000):

$$\begin{aligned}\rho\overline{u_i u_j} = {} & \frac{2}{3}\rho k\delta_{ij} - 2\mu^*_{\tau,1}S_{ij} - 2\mu^*_{\tau,2}\frac{K}{\varepsilon}(S_{ik}W_{kj} + S_{jk}W_{ki}) \\ & + 4\mu^*_{\tau,3}\frac{k}{\varepsilon}\left(S_{ik}S_{kj} - \frac{1}{3}S_{mn}S_{mn}\delta_{ij}\right)\end{aligned} \tag{4}$$

where

$$\mu^*_{\tau,i} = f_\mu \rho C^*_{\mu,i}\frac{\mathrm{k}^2}{\varepsilon} \quad \mathrm{i} = 1,2,3 \tag{5}$$

$$C^*_{\mu,1} = \alpha_1 \frac{3(1+\eta^2) + 0.2(\eta^6 + \xi^6)}{3 + \eta^2 + 6\xi^2\eta^2 + 6\xi^2 + \eta^6 + \xi^6},$$

$$C^*_{\mu,i} = \alpha_1\alpha_i \frac{3(1+\eta^2)}{3 + \eta^2 + 6\xi^2\eta^2 + 6\xi^2 + \eta^6 + \xi^6} \quad \mathrm{i} = 2,3 \tag{6}$$

and

$$\alpha_1 = 0.114, \alpha_2 = 0.187, \alpha_3 = 0.088 \tag{7}$$

The invariant coefficients are

$$\eta = \alpha_3 f_\mu \frac{k}{\epsilon}(S_{ij}S_{ij})^{0.5}, \xi = \alpha_2 f_\mu \frac{k}{\varepsilon}(W_{ij}W_{ij})^{0.5} \tag{8}$$

where the mean-strain rate and mean vorticity are

$$S_{ij} = \frac{1}{2}\left(\frac{\partial U_i}{\partial x_j} + \frac{\partial U_j}{\partial x_i}\right), W_{ij} = \frac{1}{2}\left(\frac{\partial U_i}{\partial x_j} - \frac{\partial U_j}{\partial x_i}\right) \tag{9}$$

The following equations are used for the solution of transport equations for the turbulent kinetic energy k and the turbulent dissipation rate ε,

$$\frac{\partial(\rho k)}{\partial t} + \frac{\partial}{\partial x_j}(\rho U_j k) = \frac{\partial}{\partial x_j}\left[\left(\mu + \frac{\mu_t}{\sigma_k}\right)\frac{\partial k}{\partial x_j}\right] - \rho\overline{u_i u_j}\frac{\partial U_i}{\partial x_j} - \rho\varepsilon \tag{10}$$

$$\begin{aligned}\frac{\partial(\rho\varepsilon)}{\partial t} + \frac{\partial}{\partial x_j}(\rho U_j \varepsilon) &= \frac{\partial}{\partial x_j}\left[\left(\mu + \frac{\mu_t}{\sigma_\varepsilon}\right)\frac{\partial \varepsilon}{\partial x_j}\right] \\ &- \rho C_{\varepsilon 1}\frac{\varepsilon}{k}\overline{u_i u_j}\frac{\partial U_i}{\partial x_j} - f_\varepsilon \rho C_{\varepsilon 2}\frac{\varepsilon^2}{k}\end{aligned} \tag{11}$$

where $\sigma_k = 1.4$, $\sigma_\varepsilon = 1.4$, $C_{\varepsilon 1} = 1.5$, and $C_{\varepsilon 2} = 1.9$. The turbulent eddy viscosity μ_t is calculated as

$$\mu_t = f_\mu \rho C_\mu \frac{k^2}{\varepsilon}, C_\mu = 0.09 \tag{12}$$

The damping functions are given as

$$\begin{aligned} f_\mu &= \left(1 - e^{-\frac{y^*}{14}}\right)^2 \left(1 + \frac{5}{\mathrm{Re}_t^{0.75}} e^{-\left(\frac{Re_t}{200}\right)^2}\right), f_\varepsilon \\ &= \left(1 - e^{-\frac{y^*}{3.1}}\right)^2 \left(1 - 0.3e^{-\left(\frac{\mathrm{Re}_t}{6.5}\right)^2}\right) \end{aligned} \tag{13}$$

where

$$y^* = u_\varepsilon \frac{\rho\zeta}{\mu} = \left(\frac{\mu\varepsilon}{\rho}\right)^{0.25} \frac{\rho\zeta}{\mu}, \mathrm{Re}_t = \frac{\rho k^2}{\mu\varepsilon} \tag{14}$$

and ζ is the normal distance to the nearest wall.

2.2.2 Modeling of turbulent heat flux. Two different models are used to provide closure for the turbulent heat flux terms. The first is an isotropic simple eddy diffusivity (SED) model based on the Boussinesq approximation,

$$\overline{u_j t} = -\frac{\mu_t}{\rho\sigma_T} \frac{\partial T}{\partial x_j} \tag{15}$$

where the turbulent Prandtl number for temperature σ_T is 0.89. In the second model, which is based on a generalized gradient diffusion hypothesis (GGDH), turbulent heat fluxes are dependent on both the mean temperature gradient and Reynolds stresses:

$$\overline{u_j t} = -f_\mu^T C_t \left(\overline{u_j u_k} \frac{\partial T}{\partial x_k}\right) \tag{16}$$

where $C_t = 0.3$.

Here the damping function is given as

$$f_\mu^T = (1 - e^{-0.0125\mathrm{Re_k}})^2 \left(1 + \frac{20.5}{\mathrm{Re}_t}\right) \tag{17}$$

where $\mathrm{Re}_k = \frac{\rho\sqrt{k\zeta}}{\mu}$, and Re_t is defined in Equation (14).

2.3 Boundary conditions

2.3.1 Nozzle. Two kinds of nozzle inlet boundary conditions are applied. One is the flat flow inlet, and the other is the fully developed channel flow inlet for both velocity and turbulence variables:

- *Flat inlet*

$$U = 0, V = V_{in} \tag{18}$$

Pressure is extrapolated as if the second derivative is zero. The turbulent kinetic energy and dissipation rate at the inlet are set as

$$k = \frac{3}{2}(Iv_{in})^2, \varepsilon = C_\mu \frac{k^{1.5}}{0.45B} \tag{19}$$

where I is the turbulence intensity, and B is the slot width.

- *Fully developed channel flow inlet*

At the slot jet discharge the flow is fully developed. Accordingly, a separate computation was made of developing flow in a channel and it

was continued downstream until fully developed conditions were reached. The turbulent model adopted was the same as in the main solver (see below). The computed mean velocity, kinetic energy, and dissipation profiles obtained in this preparatory calculation were interpolated on the portion of the grid for the impinging jet calculations covering the channel inlet.

2.3.2 Main channel flow inlet

$$U = U_{in}, V = 0 \tag{20}$$

Pressure is extrapolated as if the second derivative is zero. The turbulent kinetic energy and dissipation rate at the inlet are set as

$$k = \frac{3}{2}(IU_{in})^2, \varepsilon = C_\mu \frac{k^{1.5}}{0.5H} \tag{21}$$

where I is the turbulence intensity, and H is channel height.

2.3.3 Solid wall

$$U = 0, V = 0, k = 0, \varepsilon = 2\frac{\mu}{\rho}\frac{k}{\zeta^2} \tag{22}$$

Pressure is extrapolated as if the second derivative is zero.

2.4 Numerical method

An in-house computer code (Rokni, 2000), based on the finite volume technique, is modified and applied to solve the governing equations. The code uses a collocated mesh arrangement and employs the Rhie and Chow method to interpolate values of velocity at the control volume faces. The SIMPLEC algorithm couples the pressure and velocity. An algorithm based on TDMA is used for solving the equations. Convective fluxes are determined by the hybrid scheme in all equations. Under-relaxation is applied for all equations, and the proper values of the relaxation parameters for good convergence behavior were found from some test calculations. Non-uniform grids were generated, and grid refinement close to the wall was applied. Several successive grid refinements have been carried out in every considered case to get negligible effects of the mesh on the solutions. The numerical procedure is based on solving the general equation

$$\frac{\partial(\rho\Phi)}{\partial t} + \frac{\partial}{\partial x_j}(\rho U_j \Phi) = \frac{\partial}{\partial x_j}\left[\Gamma_\Phi \frac{\partial \Phi}{\partial x_j}\right] + S_\Phi \tag{23}$$

2.5 Influence of the mesh

To ensure that the turbulent fluid flow solutions are not significantly affected by the mesh, a case of Re = 20,000 with H/B = 6 and fully developed slot inlet profile, was calculated using two different numbers of grid points. The two meshes were non-uniformly spaced and had 120 × 127 and 140 × 157 grid

points, respectively. The distance from the first node off the wall for the two meshes was $y^+ = 2.6$ and 1.6 in wall units based on the maximum shear. The variation in the Nusselt number at the impingement wall for both meshes is plotted in Figure 2. The Nusselt number curves at the impingement plate for the two different meshes do not show any appreciable difference. The experimental data for the Nusselt number around the stagnation region from Lee and Lee (2000) are also enclosed to show the consistency with the simulation. Under-prediction can be identified from $x/B = 1$ to $x/B = 4$, and it is largest around $x/B = 2.5$. This can be explained from experimental uncertainties and the under-prediction of the velocity fluctuation close to the wall (Figure 5).

3. Results and discussion

Because there are no experimental data fit for heat and fluid flow of multiple impinging slot jets with cross-flow in rib-roughened channels, the computations were first validated for simplified cases against available experimental data, and then simulation in rib-roughened channels was carried out to find the optimum configuration.

3.1 Validation cases

3.1.1 Impingement

- *3.1.1.1 Fluid flow: Re = 20,000.* The experimental velocity field data of Ashforth-Frost *et al.* (1997) with $H/B = 4$ and 9.2 provide an excellent test case for the models and flow solver, since their velocity measurements near the wall are at a distance close enough to the wall to permit resolution of the shear. In the experiment, a confined and submerged air jet was used. The turbulent intensity at the nozzle was maintained at 1 per cent and the velocity at the nozzle was flat. The variation of the normalized velocity component parallel to the wall U/V_{in} with y/B was reported at several x/B positions along the impingement wall, for $H/B = 4$ (Figure 3). The distribution of the normalized velocity

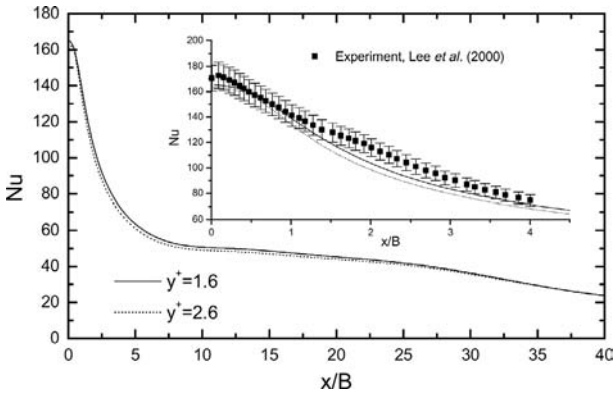

Figure 2.
Nusselt number variation with x/B for two different meshes

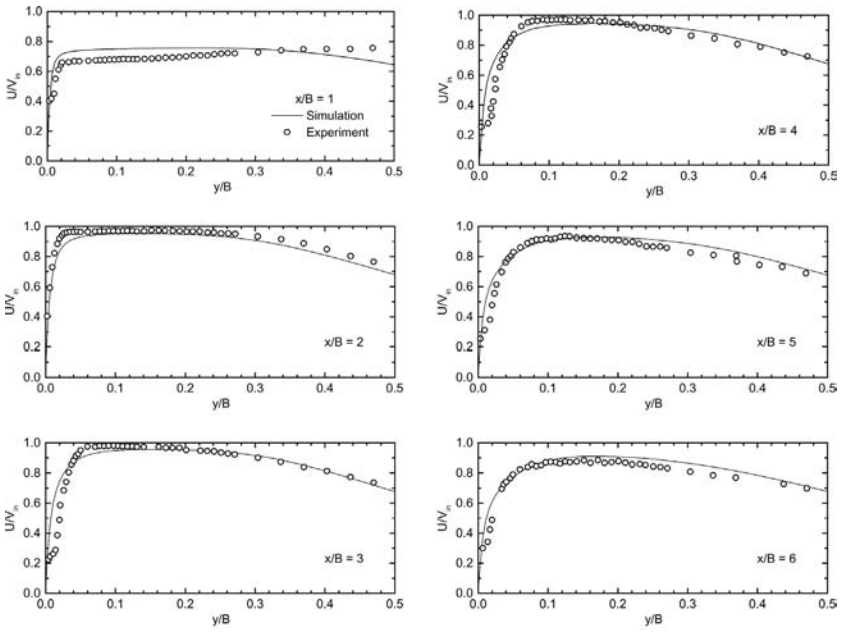

Figure 3.
Normalized velocity component parallel to the wall at different positions

Note: H/B = 4, Re = 20,000

component normal to the wall V/V_{in} with x/B was reported at several y/B positions, for H/B = 9.2 (Figure 4). The present simulations show quantitative agreement with the experimental data for both the velocity components, except at the position x/B = 1 for the velocity component parallel to the wall. It is very close to the stagnation line, and the reason is that the turbulent intensity there is somewhat over-predicted (Figure 5). Concerning the fluctuation parallel to the wall for H/B = 9.2 (Figure 5), the agreement is not so good. The fluctuation at the near wall region is under-predicted, although the mean properties are in good agreement with experiments.

- *3.1.1.2 Heat transfer: Re = 8,000 and 6,000.* The heat transfer data for one slot impinging jet of Ichimiya and Hosaka (1992) at Re = 8,000 and H/B = 1, and three slot jets at Re = 6,000 and H/B = 1 provide two good test cases for a short nozzle-to-wall distance. The computed variation in Nusselt number along the impingement wall with constant heat flux is compared in Figure 6 with the experimental data. In one jet case, the agreement is partly good. The second peak in the calculations is weak and mislocated. The under-prediction is highest at x/B = 5, up to 30 per cent. On the other hand, extremely good agreement is found at stagnation region and far downstream. The region between x/B = 3 and x/B = 9 is the developing phase of the turbulence downstream of the jet impinging on the wall. A number of authors (Gardon and Akfirat, 1966; Ashforth-Frost *et al.*, 1997) ascribed the second peak to the transition

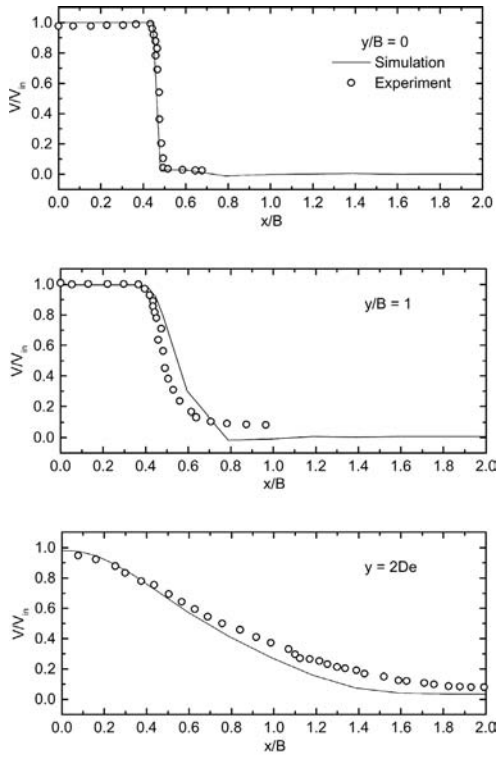

Note: H/B = 9.2, Re = 20,000

Figure 4.
Normalized velocity component normal to the wall

from laminar to turbulent boundary layers, based on their experimental evidence. EASM under-predicted this developing process, which can be understood from Figure 5. Considering the near wall region, one can observe that the fluctuation parallel to the wall is not very different from the experiments at $x/B = 1$, but the discrepancy becomes larger at $x/B = 2$, even larger at $x/B = 3$. This under-prediction of velocity fluctuation is the main reason for the under-prediction of the heat transfer coefficients between $x/B = 3$ and $x/B = 9$. Similarly, in a study of circular impingement jet by Craft *et al.* (1999), over-prediction of rms velocity component normal to the wall resulted in over-prediction of the Nusselt number. In their model, a varying C_μ was employed. It could be worthwhile to attempt to introduce this C_μ into the current EASM model, but this will be left for the future.

Because the inlet turbulence intensity is not given in the paper of Ichimiya and Hosaka (1992), five kinds of jet inlet boundary conditions were tried for this case. As expected, higher stagnation heat transfer coefficient is found with higher inlet turbulence intensity. Another interesting thing is that the highest stagnation heat transfer coefficient is obtained with fully developed channel-flow inlet boundary

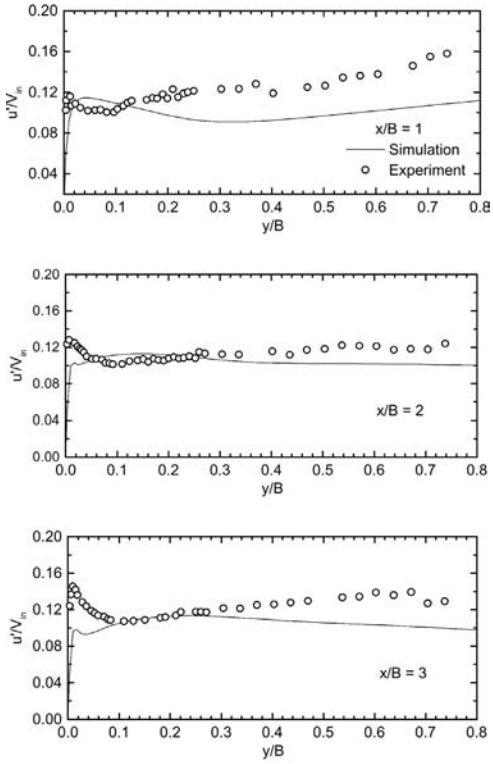

Note: H/B = 9.2, Re = 20,000

Figure 5.
Normalized velocity fluctuation parallel to the wall

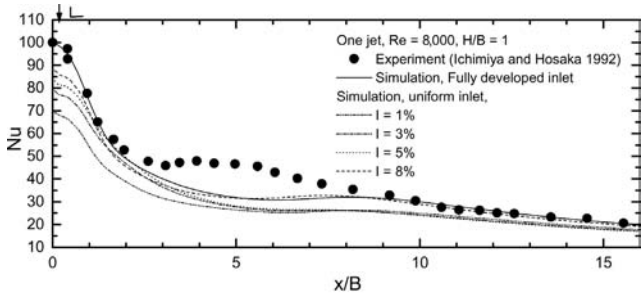

Note: One jet, H/B = 1, Re = 8,000

Figure 6.
Local Nusselt number variation with different turbulence intensity

condition, although the average inlet turbulence intensity is less than 8 per cent. This indicates that both inlet turbulence intensity and inlet velocity profile have effect on stagnation heat transfer coefficient, which is consistent with results from experiments by Lin *et al.* (1997). Therefore it is necessary to have the exact inlet turbulence intensity and velocity profile of the experiment.

In the three-jet case, two different models are used to provide closure for the turbulent heat flux terms. The vector plots are shown in Figure 7(a), and the

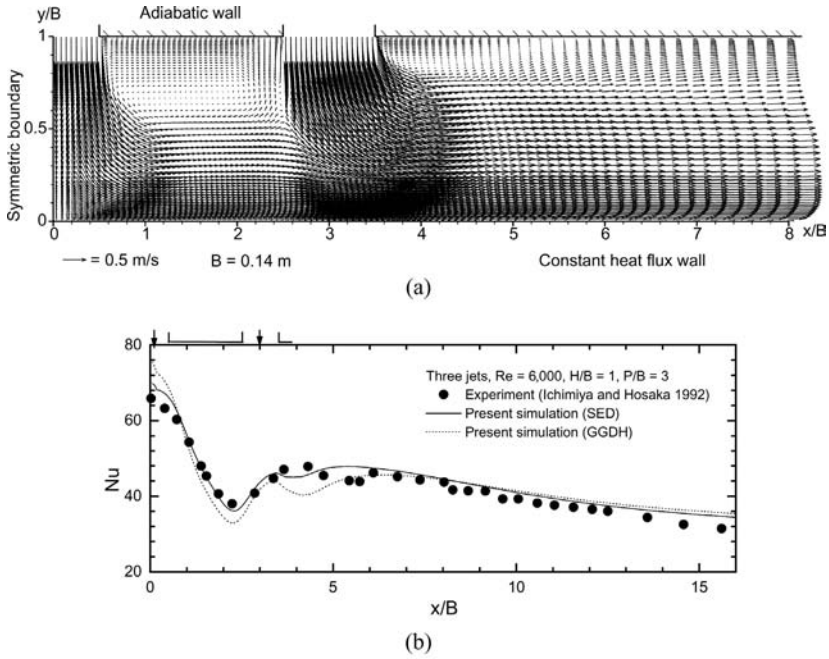

Note: For the sake of clearness, the vector plots are only shown from x/B = 0 to 8, and the total length is x/B = 18.
Three jets, H/B = 1, Re = 6,000

Figure 7.
(a) vector plots and (b) local Nusselt number variation

local Nusselt number variation is shown in Figure 7(b), along with the experimental data. Generally, the agreement is good, with three peaks, although the second and third peaks are predicted somewhat earlier and at lower values. As shown in Figure 7 (b), better agreement is achieved using SED than GGDH at most of the regions. This is another effect of the under-prediction of the velocity fluctuation, because GGDH depends on the anisotropic feature of the velocity fluctuations more strongly than SED. In other words, GGDH is more sensitive to the mal-prediction of Reynolds stresses.

3.1.2 Rib-roughened channel. The fully developed periodic heat and fluid flow in a rib-roughened channel with $H/W = 5$, $P/W = 7.2$, $E/W = 1$, and Re = 12,600 is calculated with constant heat flux boundary condition on the rib-roughened wall, while the smooth wall is insulated. The sketch of the channel configuration was depicted in Figure 1(b).

In Figure 8, the streamline contour plot is presented to show the recirculation flow and reattachment length, which plays an important role in predicting heat transfer accurately. While the big vortex is the first-kind recirculation flow induced by negative pressure gradient, two smaller vortices can be identified at the corners, which are the second-kind or stress-induced recirculations.

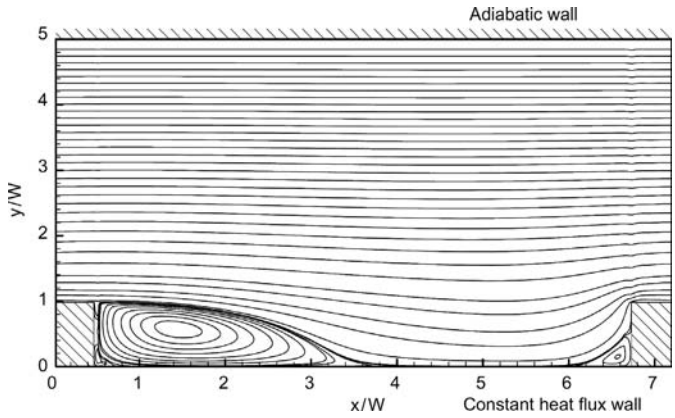

Figure 8.
Streamline contours in periodic fully developed flow in a rib-roughened channel

The local Nusselt number is normalized by the average Nusselt number for a smooth channel with $Nu_s = 0.023\mathrm{Re}^{0.8}\,\mathrm{Pr}^{0.4}$. The local Nusselt number variation is compared with the experimental data from Liu *et al.* (1993) in Figure 9, and good agreement can be identified, although the heat transfer on top of the rib is somewhat over-predicted and the minimum upstream of a rib is somewhat mislocated.

3.2 Heat and fluid flow in rib-roughened channels

The following section concerns the effect of ribs on the heat transfer coefficients along the rib-roughened wall, and to find the optimum *B/W* and rib position. During the calculations, *H/B* is set as 4, while the jet Reynolds number is 6,000 based on the slot width (*B*), and the cross-flow inlet Reynolds number is 14,000 based on the channel height (*H*). The three cases calculated are listed in Table I.

3.2.1 Heat and fluid flow of multiple jets in cross-flow without ribs. In order to provide data to compare with a rib-roughened channel, the heat and fluid flow of multiple slot jets with cross-flow was calculated. As shown in Figure 10, the existence of the cross-flow emanating from the upstream jets and channel inlet shows high effect on the flow pattern of multiple jets. One effect is the

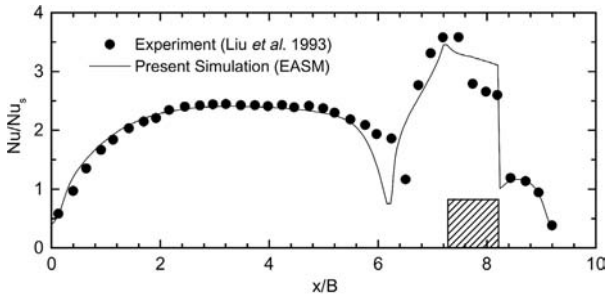

Note: W/E = 1, P/W = 7.2, Re = 12,600

Figure 9.
Local Nusselt number variation

disappearance of the stagnation region, which is important for the high heat transfer characteristics of a single impinging jet, and another is the decrease of the length of the potential core (where the velocity of the jet direction is no less than 95 per cent of the jet inlet velocity). The effect of the jets on the heat transfer characteristics is significant. The Nusselt number is almost doubled (from 50 to 100) downstream of the inlet of the second jet approximately at x/B = 13.5 (Figure 11). The explanation is twofold. First, the incoming fluid of jets increases the mean velocity of the main flow (increased mass flow), which results in higher heat transfer coefficient. Second, the jets induce recirculation, and the direct effect of the recirculation is a narrower flow passage inside the channel (Figure 10), which will accelerate the main flow and induce higher shear. In other words, the jets increase the flow velocity in the main flow direction near the wall, which results in higher velocity gradients in this region. Higher velocity gradients usually result in higher turbulence intensity, which promotes the process of heat transfer. Therefore a higher Nusselt number is obtained downstream of the inflow of the first jet. However, the heat transfer enhancement from the impinging jets will decrease with the increase of the jet number (Figure 11). The reason is that the main flow is becoming stronger and

Cases studied	Configuration	B/W	Reynolds number Jet	Reynolds number Cross-flow	Inlet profile Jet	Inlet profile Cross-flow
Case I	Multiple jets without ribs					
Case II	Figure 1(c)	1, 2, 3, 4,	6,000	14,000	Fully developed channel flow	Uniform velocity and I = 1 per cent
Case III	Figure 1(d)	5, 6, 8				

Table I. Configurations for different cases

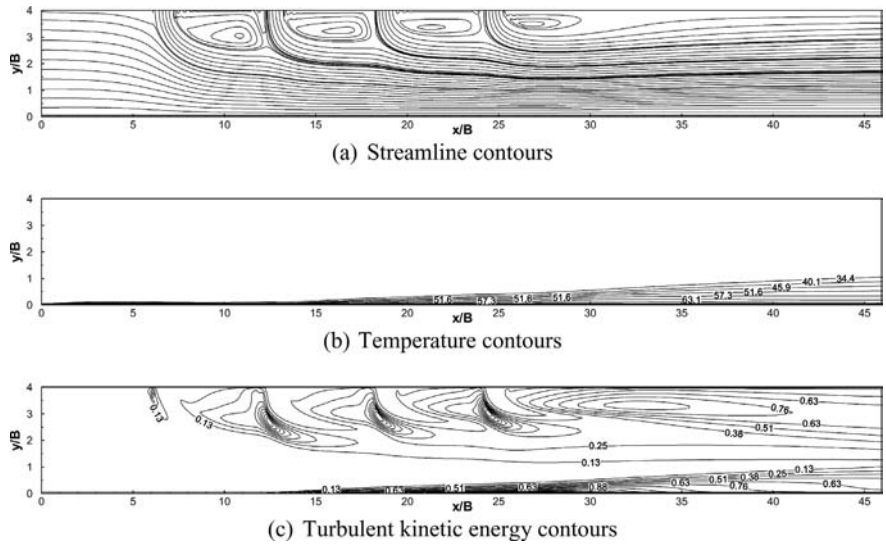

Figure 10. Streamline contour of multiple jets with cross-flow

stronger, which results in smaller and smaller recirculations downstream of the jets, and it becomes more and more difficult for the jet flow to penetrate the cross-flow and cool the wall. From another point of view, the variation of the Nusselt number can be explained from the streamline contour. The passage of the cross flow is shrinking with the inflow of the first and second jets, and this shrinking almost disappears at $x/B = 13.5$. The incoming cross-flow is deflected towards the wall as it approaches the first jet. Since the conservation of the fluid mass and constant density (due to low temperature and pressure change), the fluid from the channel inlet will be accelerated till $x/B = 13.5$. Then, the streamlines become almost flat, and the fluid will move with nearly a constant velocity near the wall until $x/B = 28$. Then, the near wall flow will be decelerated, and the temperature boundary layer grows faster. Because of the increase of the turbulence intensity, an increase of Nusselt number is found.

3.2.2 Similarity of the heat and fluid flow along a rib-roughened wall. The streamline, temperature, and turbulent kinetic energy contours of case II are displayed in Figure 12. Similarity can be identified from the streamline

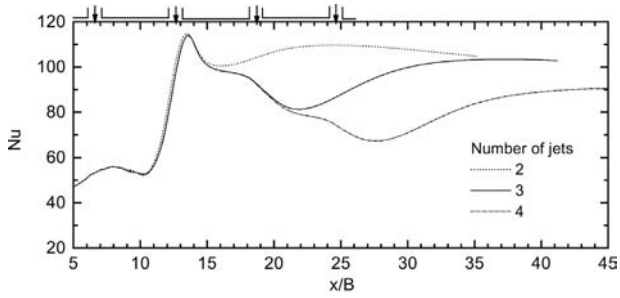

Note: H/B = 4, P/B = 6, Re = 6000

Figure 11.
Local Nusselt number variation, multiple jets with cross flow

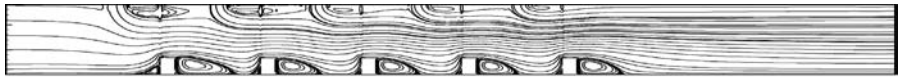

(a) Streamline contours

(b) Temperature contours

(a) Turbulent kinetic energy contours

Note: H/B = 4, B/W = 1, P/B = 6, Re = 6,000

Figure 12.
Heat and fluid flow in a rib-roughened channel for case II

contours. Nevertheless the fluid flow cannot be regarded as periodic because of the inflow of jet fluid. As shown in Figure 12(a), there is a recirculation zone downstream of each rib and jet, and there is a small recirculation at each corner, similar to that in Figure 8. Since the mean flow velocity is increasing, due to the inflow of the jet fluid, the recirculation zones downstream of the jets are becoming smaller and smaller, while the flow patterns between ribs are almost identical, except for the first. Turbulent kinetic energy is increasing with the increase of the main flow velocity and the development of the turbulence. The temperature contours are also developing in a similar way, and the bulk temperature is increasing. It is obvious that the temperature gradients perpendicular to the wall decrease in the main flow direction, and this results in the decrease of the heat transfer coefficient. The decrease of the Nusselt number is shown in Figure 13, in which similarity can be identified for different jet numbers. The values decrease but the patterns are kept identical, except at the outlet region. Since the variation of local Nusselt number does not change with an increase of jet number (Figure 13), the heat transfer characteristics are not dependent on the downstream region. Because of the similarity of the Nusselt number variation and the independence on the downstream region, channels with three jets and three ribs are selected as configuration in the study of the effect of the ribs.

3.2.3 Effect of ribs. First, let us compare the streamline contours in Figures 10 and 12. The recirculation zones induced by the jets are smaller in the rib-roughened channel. The ribs and the recirculation zones induced by the ribs served as a kind of blockage to the jet flow. This blockage prevents the main fluid flow from approaching the bottom wall, and the jet flow is oppressed (Figure 12(a)). Second, the ribs have a big effect on the temperature distribution. The temperature boundary layer in Figure 12 is thicker than in Figure 10, which is caused by the blockage effect of the ribs. Third, as expected, the turbulent kinetic energy contours are changed, and the turbulence level is higher in the channel with ribs. This means that there is a trade-off between the advantage and disadvantage of the presence of ribs, since the increase of the temperature boundary layer thickness will block the heat transfer

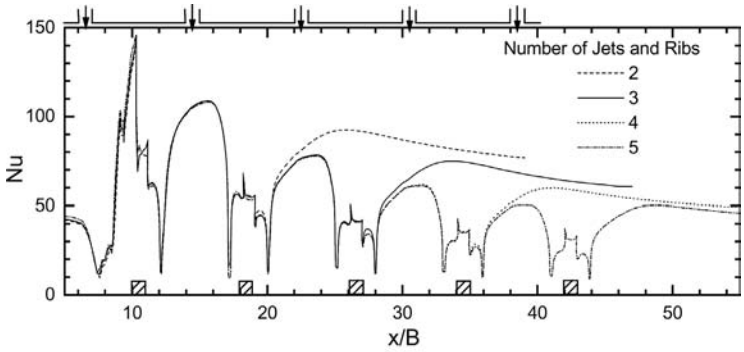

Note: H/B = 4, B/W = 1, P/B = 6, Re = 6,000

Figure 13.
Local Nusselt number variation, multiple jets with cross-flow in a rib-roughened channel

between the fluid and the wall, while the increase of the turbulence intensity will enhance the heat transfer characteristics. The local Nusselt number variation for three jets and ribs is depicted in Figure 14 along with the case for jets only. Unfortunately, the overall heat transfer coefficient is impaired by the presence of the ribs. However, this situation can be improved by rearranging the ribs and jets, as described below.

3.2.4 Effect of rib position. The recirculation induced by jets increases the velocity of main flow, but the presence of the ribs prevents the main flow from approaching the heat transfer wall. As shown in Figure 12(a), the ribs and the recirculation zones induced by the ribs serve as a kind of blockage for the jet flow, and make the jet recirculation zones smaller. A straightforward idea is to find a way to enlarge the jet recirculation zones. Because the recirculation zones induced by the jets occur between two jets, it might be helpful if the ribs are moved from the middle between two jets to be placed just below the jets, as in case III. As expected, the jet recirculation zones are enlarged due to the displacement of ribs, which can be identified in Figure 15(a). The average temperature boundary layer is becoming thinner (Figure 15(b)). The detailed comparison between case II and case III is depicted in Figure 16, at three positions. The stream-wise velocities in case III are larger than in case II close to the rib-roughened wall at positions 1 and 3, while they are similar at position 2. For the turbulent kinetic energy, the situation is consistent with the stream-wise velocity. Temperature gradients are higher in case III than in case II at the three positions, which result in enhancement of heat transfer (Figure 17). The

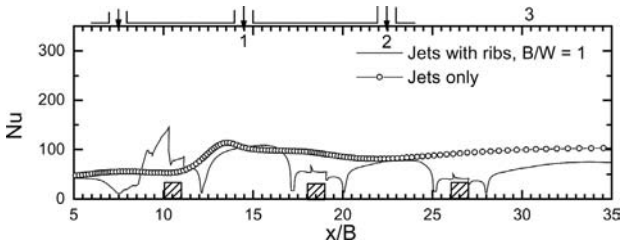

Figure 14.
Local Nusselt number variation, multiple jets with cross-flow in a rib-roughened channel

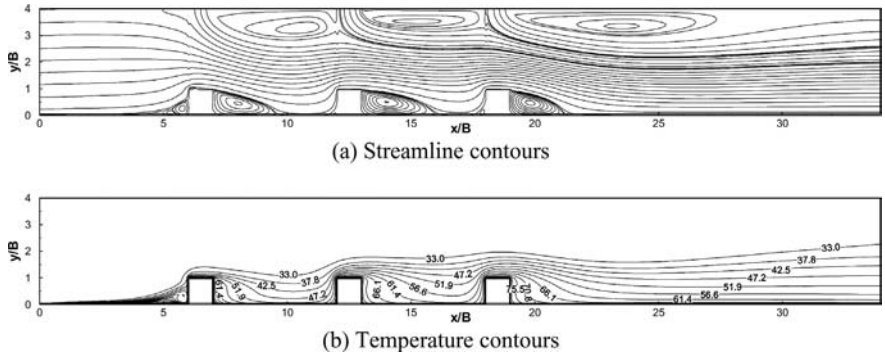

Figure 15.
Heat and fluid flow in a rib-roughened channel for case III

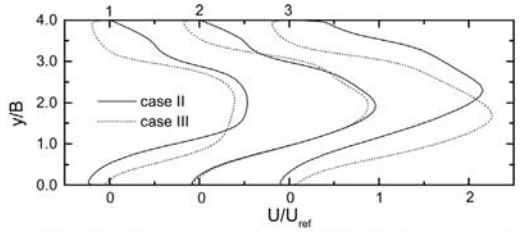

(a) Velocity component parallel to the bottom wall

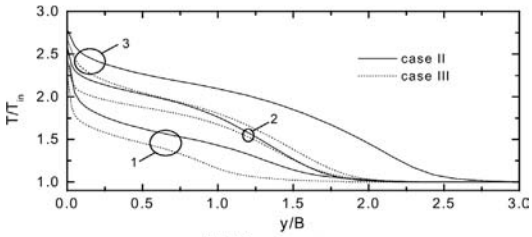

(b) Temperature

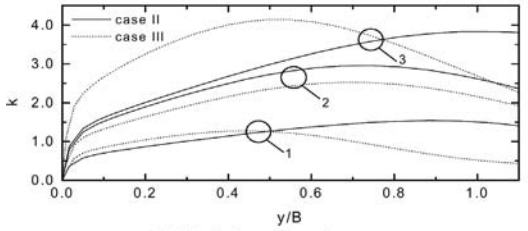

(c) Turbulent kinetic energy

Note: Position 1 represents the middle between the first and second ribs, and Position 2 represents the middle between the second and third ribs, and so on.

Figure 16.
Comparison between case II and case III for $B/W = 1$. Position 1 represents the middle between the first and second ribs, and position 2 represents the middle between the second and third ribs, and so on

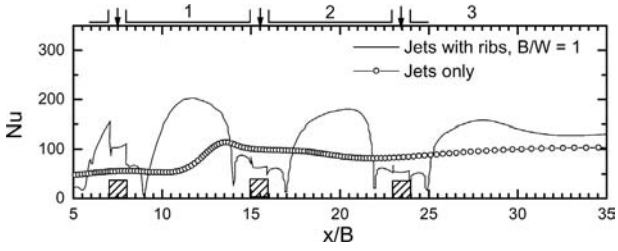

Figure 17.
Local Nusselt number variation, multiple jets with cross-flow in a rib-roughened channel

Nusselt number is almost doubled. Higher Nusselt number is obtained for case III than for case II when $B/W \leq 3$, but the contrary is true when $B/W > 3$ (Figure 18). The reason is that the turbulence intensity level induced by the ribs will be the dominating mechanism as the rib size is decreased. In case II, the ribs are located at the middle between two jets, where the main velocities are

the highest, so higher turbulence intensity is induced in case II than in case III, which results in higher heat transfer coefficient when the rib size becomes smaller.

3.2.5 Effect of ratio between jet width and rib width. Calculations have been carried out for seven different *B/W*s from 1 to 8, while all other parameters were fixed. The average Nusselt number variation vs *B/W* is displayed in Figure 18 for cases II and III along with that for case I. For case II, the average Nusselt number in the rib-roughened channel is lower than that in the smooth channel (case I), when *B/W* is unity. The situation is changed when $B/W = 2$, and the average Nusselt number is even higher for $B/W = 3$. However, the average Nusselt number will decrease with the increase of *B/W* beyond $B/W > 4$ (Figure 18). For case III, a similar variation can be identified, except that the start of decrease is at $B/W = 3$, while it is $B/W = 4$ for case II. Because of the disturbance of the ribs, higher turbulence intensity is induced, which results in higher heat transfer coefficient (Figure 17). On the other hand, the ribs and recirculation zones between the ribs prevent the main flow from approaching the bottom wall, and a lower heat transfer coefficient will be obtained if the blockage is strong enough (Figure 14). However, with the increase of *B/W*, the situation will be changed again (Figure 18), because the ribs cannot induce sufficient turbulence any more, as they are too small. The heat transfer enhancement will decrease with the decrease of rib size. The limit of a rib-roughened wall is a smooth wall, if the rib size is approaching zero.

4. Conclusions

The explicit algebraic stress model used in the present study is effective in predicting heat and fluid flow both in impingement jet and in rib-roughened channels, as shown in the simplified cases for validation. For heat flux modeling, better performance is achieved by using SED rather than GGDH, due to the under-prediction of the velocity fluctuations at the near wall region, and this needs further consideration.

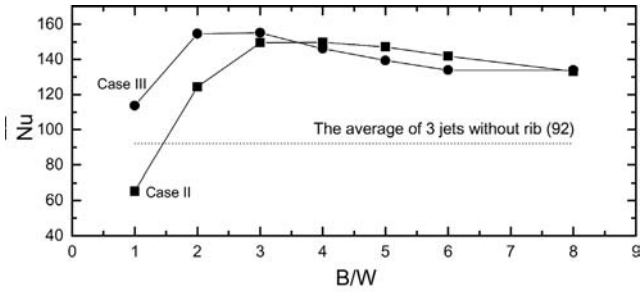

Note: H/B = 4, P/B = 6, Re = 6,000, number of jets and ribs is three

Figure 18.
Average Nusselt number variation versus *B/W*

The inlet boundary conditions, including turbulence intensity and velocity profile, has a very significant effect on the heat and fluid flow characteristics of a turbulent impinging jet.

The heat and fluid flow of multiple impinging jets in a rib-roughened channel with $P/W = 6$ have been studied. The ribs enhance the heat transfer, if they are well arranged. Both the position and size of the ribs are of importance for heat transfer in rib-roughened channel. Best performance is found when $B/W = 4$ for case II, while $B/W = 3$ for case III.

The size of the recirculation zones induced by the jets plays an important role in the heat transfer characteristics near the roughened wall. Larger recirculation zones result in higher heat transfer coefficients.

Additional work is needed for better understanding of the heat and fluid flow behavior of multiple impingement jets in a rib-roughened channel, and the effects of *B/H, P/B*, number of jets and ribs, and different configuration of flow rate from the channel inlet and the jets have to be revealed.

References and further reading

Ashforth-Frost, S., Jambunathan, K. and Whitney, C.F. (1997), "Velocity and turbulence characteristics of a semi-confined orthogonally impinging slot jet", *Exp. Thermal and Fluid Science*, Vol. 14 No. 1, pp. 60-7.

Chen, Q. and Modi, V. (1999), "Mass transfer in turbulent impinging slot jets", *Int. J. Heat Mass Transfer*, Vol. 42 No. 5, pp. 873-87.

Craft, T.J., Graham, L.J.W. and Launder, B.E. (1993), "Impinging jet studies for turbulence model assessment – II. An examination of the performance of four turbulence models", *Int. J. Heat Mass Transfer*, Vol. 36 No. 10, pp. 2685-97.

Craft, T.J., Iacovides, H. and Yoon, J.H. (1999), "Progress in the use of non-linear two-equation models in the computation of convection heat-transfer in impinging and separated flows", *Flow, Turbulence and Combustion*, Vol. 63, pp. 59-80.

Durbin, P.A. (1995), "Separated flow components with k-ε-v^2 model", *AIAA J.*, Vol. 33 No. 4, pp. 659-64.

Gardon, R. and Akfirat, J.C. (1966), "Heat transfer characteristics of impinging two-dimensional air jets", *ASME J. Heat Transfer*, Vol. 88, February, pp. 101-8.

Gatski, T.B. and Speziale, C.G. (1993), "On explicit algebraic stress models for complex turbulent flows", *J. Fluid Mech.*, Vol. 254, pp. 59-78.

Ichimiya, K. and Hosaka, N. (1992), "Experimental study of heat transfer characteristics due to confined impinging two-dimensional jets", *Exp. Thermal and Fluid Science*, Vol. 5 No. 6, pp. 803-7.

Lee, J. and Lee, S.J. (2000), "The effect of nozzle configuration on stagnation region heat transfer enhancement of axisymmetric jet impingement", *Int. J. Heat Mass Transfer*, Vol. 43 No. 18, pp. 3497-509.

Lin, Z.H., Chou, Y.J. and Hung, Y.H. (1997), "Heat transfer behaviors of a confined slot jet impingement", *Int. J. Heat Mass Transfer*, Vol. 40 No. 5, pp. 1095-107.

Liu, T.M., Hwang, J.J. and Chen, S.H. (1993), "Simulation and measurement of enhanced turbulent heat transfer in a channel with periodic ribs on one principal wall", *Int. J. Heat Mass Transfer*, Vol. 36 No. 2, pp. 507-17.

Looney, M.K. and Walsh, J.J. (1984), "Mean-flow and turbulent characteristics of free and impinging jet flows", *J. Fluid Mech.*, Vol. 147, pp. 397-429.

Rokni, M. (2000), "A new low-Reynolds version of an explicit algebraic stress model for turbulent convective heat transfer in ducts", *Numerical Heat Transfer*, Part B, Vol. 37 No. 3, pp. 331-63.

Saidi, A. and Sundén, B. (2000), "Numerical simulation of turbulent convective heat transfer in square ribbed ducts", *Numerical Heat Transfer*, Part A, Vol. 38 No. 1, pp. 67-88.

Seyedein, S.H., Hasan, M. and Mujumdar, A.S. (1995), "Turbulent flow and heat transfer from confined multiple impinging slot jets", *Numerical Heat Transfer*, Part A, Vol. 27 No. 1, pp. 35-51.

Tsai, W.B., Lin, W.W. and Chieng, C.C. (2000), "Computation of enhanced turbulent heat transfer in a channel with periodic ribs", *Int. J. Numerical Methods for Heat & Fluid Flow*, Vol. 10 No. 1, pp. 47-66.